

PHOTONICS Research

Synthetic aperture ptychography: coded sensor translation for joint spatial-Fourier bandwidth expansion

PENGMING SONG,[†] SHAOWEI JIANG,[†] TIANBO WANG, CHENGFEI GUO,  RUIHAI WANG, TERRANCE ZHANG, AND GUOAN ZHENG*

Department of Biomedical Engineering, University of Connecticut, Storrs, Connecticut 06269, USA

*Corresponding author: guoan.zheng@uconn.edu

Received 7 April 2022; revised 15 May 2022; accepted 15 May 2022; posted 16 May 2022 (Doc. ID 460549); published 21 June 2022

Conventional ptychography translates an object through a localized probe beam to widen the field of view in real space. Fourier ptychography translates the object spectrum through a pupil aperture to expand the Fourier bandwidth in reciprocal space. Here we report an imaging modality, termed synthetic aperture ptychography (SAP), to get the best of both techniques. In SAP, we illuminate a stationary object using an extended plane wave and translate a coded image sensor at the far field for data acquisition. The coded layer attached on the sensor modulates the object exit waves and serves as an effective ptychographic probe for phase retrieval. The sensor translation process in SAP synthesizes a large complex-valued wavefront at the intermediate aperture plane. By propagating this wavefront back to the object plane, we can widen the field of view in real space and expand the Fourier bandwidth in reciprocal space simultaneously. We validate the SAP approach with transmission targets and reflection silicon microchips. A 20-mm aperture was synthesized using a 5-mm sensor, achieving a four-fold gain in resolution and 16-fold gain in field of view for object recovery. In addition, the thin sample requirement in ptychography is no longer required in SAP. One can digitally propagate the recovered exit wave to any axial position for post-acquisition refocusing. The SAP scheme offers a solution for far-field sub-diffraction imaging without using lenses. It can be adopted in coherent diffraction imaging setups with radiation sources from visible light, extreme ultraviolet, and X-ray, to electron. © 2022 Chinese Laser Press

<https://doi.org/10.1364/PRJ.460549>

1. INTRODUCTION

Ptychography is a coherent diffraction imaging (CDI) technique that has grown rapidly in the past years [1,2]. The original concept was developed to address the missing phase challenge in crystallography [3]. By translating a narrow coherent probe beam on a crystalline specimen, it aspires to extract the phase of Bragg peaks from far-field diffraction patterns. The modern form of this technique was brought to fruition by adopting an iterative phase retrieval framework [4]. Experiment procedures remain the same, where a specimen is laterally translated through a spatially confined probe beam and the diffraction patterns are recorded at the far field. Using the phase retrieval framework, the reconstruction process iteratively imposes two different constraints during the object scanning process: first, the diffraction measurements serve as the Fourier magnitude constraints in reciprocal space; second, the confined probe beam limits the physical extent of the object for each measurement and serves as the support constraint in real space. Ptychography requires no imaging optics downstream of a specimen under investigation. It inherently generates both

intensity and phase contrast for quantitative investigation of material properties—a capability that many competing imaging modalities lack. The data redundancy of ptychography further allows it to recover other important system information, including the illumination probe beam [5–8], multiple coherent modes of the probe beam or the object [9], images at different spectral channels [10–12], multiple depth sections of a 3D object [13], diffraction data beyond the detector size [14], and orthogonal modes of an unstable illumination beam [15], among others. In the past decade, lensless ptychography has captured widespread interest from different imaging communities. In the field of biomedical imaging, it has been demonstrated for optofluidic flow-cytometer screening [16], urine sediment testing [17], blood analysis [17,18], malaria parasite screening [19], high-throughput digital pathology [19], antibiotic susceptibility testing [20], microbial limit testing [20], and large-scale yeast cell culture monitoring [21], among others. In the field of X-ray optics and extreme ultraviolet (EUV) imaging, it has become an indispensable modality in most synchrotrons and national laboratories worldwide [22,23]. Given that

the brightness of coherent X-ray sources is expected to increase by orders of magnitude in the coming years, lensless ptychography has a promising future in imaging different non-crystalline structures on an atomic scale.

Ptychography can also be implemented using a lens-based system. Fourier ptychography (FP) is one example that swaps real space and reciprocal space using a lens [24]. In a typical FP implementation, an LED array is used to illuminate an object from different incident angles, and a low-numerical-aperture (NA) objective lens is used to acquire the corresponding low-resolution images. At each illumination angle, the captured image corresponds to the information of a circular aperture in Fourier space. The object scanning process in conventional ptychography is now implemented by the angular scanning process in FP for Fourier aperture synthesizing. The recovered spectrum in the reciprocal space of FP is then transformed back to the spatial domain to obtain a high-resolution, large-field-of-view object image with both intensity and phase properties. By combining with diffraction tomography, FP can also recover the scattering potential of 3D objects [25,26]. One surprising development of FP is a camera-scanning scheme that deviates from microscopy and enables far-field sub-diffraction imaging [27–29]. In this scheme, a lens–detector combo is translated at the far field for image acquisition. Far-field propagation of a coherent light field corresponds to the operation of a Fourier transform. Therefore, the entrance pupil of the lens naturally serves as a circular support constraint in reciprocal space. The lens then performs a second Fourier transform to convert the spectrum back to real space for imaging. By moving the entire lens–detector combo to different positions at the far field, one can acquire low-resolution images corresponding to different circular apertures in reciprocal space. These images can then be synthesized in a manner seen in FP. The size of the lens aperture does not limit the final image resolution. Instead, the resolution is determined by how far one can translate the camera.

In brief, conventional lensless ptychography scans an object in real space to widen the field of view. Lens-based FP scans the object spectrum in reciprocal space to expand the spatial-frequency bandwidth. These two modalities are mathematically equivalent if we treat the object spectrum in FP as the real-space object in conventional ptychography. Here we report an imaging scheme that merges the benefits of both techniques. This new scheme, termed synthetic aperture ptychography (SAP), is a lensless modality for far-field sub-diffraction imaging. Instead of translating the specimen over a confined probe beam, we illuminate the entire stationary object using an extended plane wave in SAP. A coded image sensor is then translated at the far field for *in situ* or *in operando* data acquisition. The coded mask attached on the sensor modulates the diffractive light waves from the object and serves as an effective ptychographic probe for object recovery. Once characterized, the coded mask remains unchanged for all subsequent experiments, addressing the blind ptychography problem where both the object and probe are unknown. The sensor translation process in SAP synthesizes a large complex-valued wavefront at the intermediate aperture plane. By propagating this wavefront back to the object plane, we can widen the field of view in real space and

expand the spatial-frequency bandwidth in reciprocal space, thereby achieving an optimal combination of benefits from both conventional ptychography and FP. In the operation of conventional ptychography and FP, a multiplication process is used to model the interaction between the object and the incident beam on the object. This requires the object to be optically thin. In SAP, the restriction on specimen thickness is waived because the thin sample requirement has been converted into the thin coded layer requirement on the image sensor. The recovered exit wave can be digitally propagated to any axial position for post-measurement refocusing. SAP modality offers a simple solution for sub-diffraction imaging via reference-free aperture synthesizing. The lensless nature of this modality further allows it to be implemented in a variety of CDI setups with radiation sources from visible light, ultraviolet, and X-rays, to electrons.

2. SYNTHETIC APERTURE PTYCHOGRAPHY

A. Concept and Operation of SAP

Drawing connections and distinctions within related modalities helps clarify the concept of the SAP approach. Figure 1 summarizes the differences between conventional ptychography and SAP. For both approaches, an object is placed in the spatial domain, and a detector is placed at the far field for diffraction data acquisition. When the detector is placed in the Fraunhofer zone with a Fresnel number $\ll 1$, a Fourier transform (denotes as “*FT*” in Fig. 1) can approximate the light propagation from the object plane to the detector plane. In such cases, the detector is effectively placed in reciprocal space defined by the wave-number coordinates (k_x, k_y) in Fig. 1. However, the Fraunhofer approximation implies a significantly long distance in between the object and the detector. For conventional bench-top setups, the Fresnel number is on the order of one, and it does not satisfy the aforementioned Fraunhofer approximation condition. Light propagation from the object plane to the detector plane can be approximated using a Fresnel diffraction calculation instead (denoted as “*prop*” in Fig. 1).

For conventional ptychography, the confined probe beam $\text{Probe}(x, y)$ interacts with the translated object $O(x - x_i, y - y_i)$, and the resultant light waves propagate for a distance d to the detector plane. The image sensor then registers the intensity of the light waves on the pixel array. The images captured at the far field are used during the reconstruction process to update the corresponding confined regions in real space, as shown in the system configuration panel in Fig. 1. In this modality, object translation effectively widens the imaging field of view in real space. The spanning angle of the detector determines the achieved resolution. Furthermore, an object overlap in between adjacent scan positions is critical to the reconstruction process. Adequate overlap allows each point of the object to be visited multiple times in the captured diffraction data, thus providing a sufficiently redundant set of measurements for phase retrieval. If no overlap is imposed, the recovery process is carried out independently for each acquisition, leading to the usual ambiguities inherent to the phase problem.

For SAP, we illuminate the entire object with an extended plane wave. The exit waves from the object propagate for a distance d_1 and reach the coded layer plane on the image sensor.

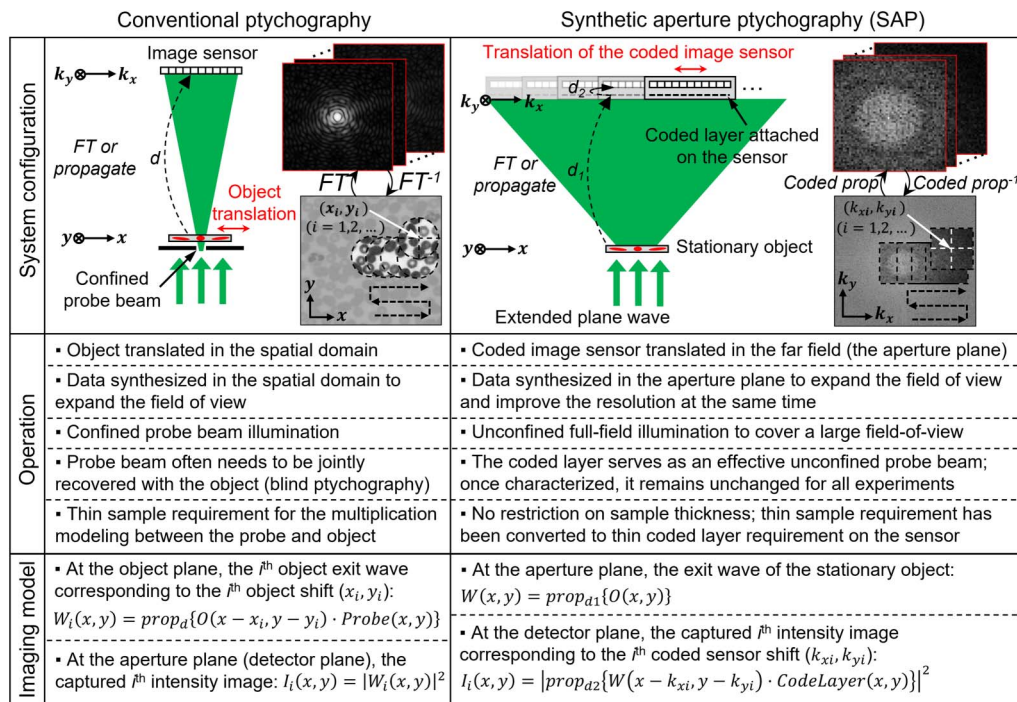


Fig. 1. Comparison between conventional ptychography and SAP. Conventional ptychography translates the object over a confined probe beam in the spatial domain and acquires diffraction data at the far field. During the reconstruction process, conventional ptychography stitches the information in the spatial domain to expand the field of view. SAP illuminates the stationary object with an extended plane wave and translates a coded sensor at the far field for data acquisition. In the reconstruction process, SAP stitches the information in the intermediate aperture plane for object recovery. It can widen the field of view in real space and expand the spatial-frequency bandwidth in reciprocal space at the same time. The dashed arrows present free-space propagation over certain distances.

The transmission profile of the coded layer modulates the object exit waves in a point-wise multiplication process, similar to the object-probe interaction in conventional ptychography. Therefore, the coded layer in SAP can be treated as an unconfined probe beam for ptychographic reconstruction. The resultant modulated light waves then propagate for a small distance d_2 and reach the pixel array for intensity detection. In the reconstruction process, SAP iteratively stitches the information at the plane of the coded layer. If the detector is placed at the Fraunhofer zone, it effectively performs aperture synthesizing in reciprocal space, like that in FP. If the detector is placed in the Fresnel zone, the reconstruction process effectively synthesizes a large complex-valued wavefront at the intermediate aperture plane (i.e., at the plane of the coded layer). By propagating this wavefront back to the object plane, we can simultaneously widen the imaging field of view and expand the Fourier bandwidth. If no coded layer is attached on the image sensor, the acquired images in SAP are equivalent to one far-field diffraction measurement using a large detector. Due to the absence of the object-probe modulation process, ptychographic reconstruction cannot be achieved.

The advantages and unique properties of the SAP scheme can be summarized as follows. First, SAP stitches the information at the intermediate aperture plane when the detector is placed in the Fresnel zone. It can widen the imaging field of view and expand the Fourier bandwidth at the same time, getting the best of both conventional ptychography and FP.

Second, the confined illumination probe beam in conventional ptychography often varies for different experiments. Therefore, the probe beam needs to be jointly recovered with the object in the reconstruction process (also termed blind ptychography [5–8]). In contrast, SAP adopts a fixed coded layer on the image sensor that, once characterized, remains unchanged for all subsequent experiments. Third, conventional ptychography uses a point-wise multiplication process to model the interaction between the object and the structured probe beam. This process is valid only when the sample is thin. The thickness limit for this approximation has been theoretically studied via different means [30,31]. In SAP, the object-probe multiplication process is performed at the coded layer plane. Therefore, the thin sample requirement in conventional ptychography is converted into a thin coded layer requirement in SAP [32], thus rendering the object thickness irrelevant to the reconstruction process. After recovery, one can digitally propagate the recovered object wavefront to any axial position for post-measurement refocusing [21,27,32]. Last, interferometric setups perform aperture synthesizing using a reference wave [33]. Such schemes require light sources with high spatial and temporal coherence. The associated optical setups are often subjected to vibration and other interferometry-related challenges. The reported SAP, on the other hand, requires neither interferometric measurements nor reference waves. It can be implemented with low-coherence sources such as X-ray and EUV sources, LEDs, and electrons. The lensless nature further makes it comparable

to a variety of CDI setups that are generally limited by poor and aberrative lens elements.

B. Imaging Model and Reconstruction Process of SAP

In this section, we discuss the forward imaging model and the reconstruction process of SAP. As shown in the right panel of Fig. 1, the complex wavefront $W(x, y)$ at the intermediate aperture plane can be written as the object exit wave $O(x, y)$ propagates for a distance d_1 :

$$W(x, y) = O(x, y) \otimes \text{PSF}_{\text{free}}(d_1). \quad (1)$$

PSF_{free} in Eq. (1) represents the Fresnel propagation kernel, and “ \otimes ” denotes the convolution operation. At the intermediate aperture plane, the complex wavefront $W(x, y)$ is modulated by the coded layer $\text{CL}(x, y)$ on the detector, and the resultant signal propagates for a small distance d_2 to the plane of the pixel array. In the bottom right panel of Fig. 1, we use (k_{xi}, k_{yi}) to represent the i th translational shift of the coded sensor at the Fraunhofer zone. Without loss of generality, we assume that the coded sensor is placed at the Fresnel zone for the rest of paper. We use (x_i, y_i) to represent the i th translational shift of the coded sensor at the intermediate aperture plane. Thus, the acquired image $I_i(x, y)$ can be written as

$$I_i(x, y) = |[W(x - x_i, y - y_i) \cdot \text{CL}(x, y)] \otimes \text{PSF}_{\text{free}}(d_2)|^2, \quad (2)$$

where “ \cdot ” represents point-wise multiplication. We note that the image dimensions in Eq. (1) are different from those in

Eq. (2). In Eq. (1), the complex wavefront at the intermediate aperture plane $W(x, y)$ and the object exit wave $O(x, y)$ have an image dimension of $M \times N$ pixels. In contrast, the captured image $I_i(x, y)$ and the coded layer profile $\text{CL}(x, y)$ have a smaller image dimension of $m \times n$ pixels. The reconstruction process of SAP aims to synthesize a significantly larger image with $M \times N$ pixels at the intermediate aperture plane based on the raw captured measurements with $m \times n$ pixels. In our experiment, we set $M = 5m$ and $N = 5n$. The enhancement factor of five is determined by the maximum translational shift of the coded sensor at the intermediate aperture plane. The final achievable resolution is not limited by the spanning angle of the detector. Instead, it is determined by the spanning angle of the synthesized wavefront at the intermediate aperture plane ($r = \lambda/\text{NA}_{\text{syn}}$, where r is the resolution limit of SAP, λ is the wavelength, and NA_{syn} is the synthetic NA of the translated coded sensor).

Figure 2 shows the reconstruction process of SAP. We first initialize the object exit wavefront $W(x, y)$ and the coded layer $\text{CL}(x, y)$ in lines 1 and 2. In line 5, we crop a sub-region of the wavefront $W(x, y)$ corresponding to the coded sensor shift (x_i, y_i) . During this operation, the image size is reduced from $M \times N$ pixels to $m \times n$ pixels. In line 6, we match the cropped wavefront in the intermediate aperture plane by performing a sub-pixel shift of the coded layer profile. In line 7, the cropped wavefront is modulated by the coded layer via a multiplication process. The resultant light wave is propagated to the plane of

Reconstruction process of synthetic aperture ptychography (SAP)

Input: Captured images $I_i(x, y)$ ($i = 1, 2, \dots, I$) by translating the coded sensor to different positions (x_i, y_i) s, the distance between the object and the coded layer d_1 , the distance between the coded layer and the pixel array d_2 , and (x_i, y_i) s.

Output: Wide field-of-view, high-resolution object $O(x, y)$ and the coded layer $\text{CL}(x, y)$ (in the calibration experiment only)

Note on image dimensions: The captured images $I_i(x, y)$ and coded layer on the sensor $\text{CL}(x, y)$ have an image dimension of $m \times n$ pixels. The object $O(x, y)$ at the spatial domain and the object wavefront $W(x, y)$ at the coded layer plane have an image dimension of $M \times N$ pixels. Here M, N, m, n are even number and $M = 5m$, $N = 5n$ in our implementation.

1. Initialize the object exit wavefront $W(x, y)$ ($x = 1, 2, \dots, M; y = 1, 2, \dots, N$) at the coded layer plane.
2. Initialize the coded layer profile $\text{CL}(x, y)$ ($x = 1, 2, \dots, m; y = 1, 2, \dots, n$) at the coded layer plane.
3. for $t = 1: T$ (different iterations)
 4. for $i = 1: I$ (different captured images)
 5. $w_i(x, y) = W\left(x + \frac{M-m}{2} + [x_i], y + \frac{N-n}{2} + [y_i]\right)$ % Crop a sub-region from the wavefront $W(x, y)$,
 $x = 1, 2, \dots, m; y = 1, 2, \dots, n$; “[\cdot]”: the floor function
 6. $\text{CL}_i(x, y) = \text{CL}(x - (x_i - [x_i]), y - (y_i - [y_i]))$ % Shift the coded layer by $(x_i - [x_i], y_i - [y_i])$
 7. $\phi_i(x, y) = \text{CL}_i(x, y) \cdot w_i(x, y)$ % Exit wave on the coded layer plane
 8. $\phi_i(x, y) = \text{PSF}_{\text{free}}(d_2) * \phi_i(x, y)$ % Modulated light wave on the image sensor plane
 9. Update $\phi_i(x, y)$ based on the i th measurement:

$$\phi_i^{\text{update}}(x, y) = \phi_i(x, y) \cdot \frac{\sqrt{I_i(x, y)}}{|\phi_i(x, y)|}$$
 % Replace the amplitude with the raw image $\sqrt{I_i(x, y)}$
 10. $\phi_i^{\text{update}}(x, y) = \text{PSF}_{\text{free}}(-d_2) * \phi_i^{\text{update}}(x, y)$ % Propagate back to the coded layer plane
 11. Jointly update the sub-region wavefront $w_i(x, y)$ and the shifted coded layer profile $\text{CL}_i(x, y)$:

$$\text{CL}_i^{\text{update}}(x, y) = \text{CL}_i(x, y) + \frac{\text{conj}(w_i(x, y)) \cdot \{\phi_i^{\text{update}}(x, y) - \phi_i(x, y)\}}{(1 - \alpha_s)|w_i(x, y)|^2 + \alpha_s|w_i(x, y)|_{\text{max}}^2}$$

$$w_i^{\text{update}}(x, y) = w_i(x, y) + \frac{\text{conj}(\text{CL}_i(x, y)) \cdot \{\phi_i^{\text{update}}(x, y) - \phi_i(x, y)\}}{(1 - \alpha_w)|\text{CL}_i(x, y)|^2 + \alpha_w|\text{CL}_i(x, y)|_{\text{max}}^2}$$
 12. $\text{CL}(x, y) = \text{CL}_i^{\text{update}}(x + (x_i - [x_i]), y + (y_i - [y_i]))$ % Shift back the coded layer profile
 13. $W\left(x + \frac{M-m}{2} + [x_i], y + \frac{N-n}{2} + [y_i]\right) = w_i^{\text{update}}(x, y)$ % Update the sub-region of the wavefront
 14. end
 15. end
 16. $O(x, y) = \text{PSF}_{\text{free}}(-d_1) * W(x, y)$ ($x = 1, 2, \dots, M; y = 1, 2, \dots, N$)

Fig. 2. Reconstruction process of SAP. The acquired images are used to update the specific regions of the exit wavefront $W(x, y)$ at the intermediate aperture plane. After recovery, we backpropagate the exit wavefront to the object plane for image recovery. The object reconstruction process of SAP can widen the imaging field of view in real space and expand the Fourier spectral bandwidth in reciprocal space at the same time.

the pixel array in line 8. In line 9, we update the light wave using the measured amplitude. In line 10, we propagate the updated wave back to the coded layer plane. In line 11, we update the coded layer and the cropped wavefront using the mPIE routine [34]. We note that the coded layer is updated only in the calibration experiment. In line 12, the updated coded layer is shifted back by the sub-pixel amount defined in line 6. In line 13, the cropped sub-region wavefront is used to update the corresponding region of $W(x, y)$. In line 14, the process is repeated for all measurements with different positional shifts of the coded sensor. In line 15, the process is iterated until the solution converges. Last, we propagate the synthesized wavefront from the intermediate aperture plane to the object plane, obtaining a reconstruction with a widened field of view and an expanded spectral bandwidth at the same time.

3. RESULTS

We validated the SAP approach with the object transmission and reflection configurations shown in Figs. 3(a) and 3(b). We illuminated the sample using a collimated 532-nm laser beam for both configurations. The coded mask on the image sensor was created by coating the sensor's cover glass with microbeads. The size of the microbeads is 1–2 μm in diameter. This thin and dense coded layer allows the modulation process to be approximated by point-wise multiplication between the wavefront $W(x, y)$ and the coded layer profile $CL(x, y)$ [30]. Figure 3(c) shows the design of the coded image sensor, where the size of the coded mask is smaller than the size of the active pixel array. We created two clear regions by removing the coded layer on the sensor's cover glass. The captured images through these two clear regions were used for tracking the positional shift of the coded sensor. The top ~ 250 rows in Fig. 3(c) were used for positional tracking in the x direction. The right ~ 600 columns were used for positional tracking in the y direction. Figure S1 in Ref. [35] shows the coded image sensor used in our experiments. Figure S2 in Ref. [35] shows the recovered amplitude and phase profiles of the coded layer on the image

sensor. Once characterized, the coded mask remains unchanged for all subsequent experiments.

For the transmission configuration in Fig. 3(a), we scanned the coded sensor in the Fresnel zone with $d_1 = 100$ mm. The size of the modulated region is 5 mm \times 5 mm, with a pixel size of 1.85 μm (2700 \times 2700 pixels for each image modulated by the coded layer). The distance between the coded layer and the pixel array is 840 μm . We translated the coded sensor using a motorized x - y stage. The size of the final synthetic image is 20 mm \times 20 mm at the intermediate aperture plane. Once the complex wavefront was recovered at this plane, we propagated it back to the object plane for image recovery. Figure 3(b) shows the reflection configuration of SAP. In this scheme, we illuminated the reflective sample at a 20° incident angle. The coded sensor was then translated at the plane perpendicular to the zero-order reflective beam. The recovered wavefront at the coded layer plane is then propagated back to the object plane, with a tilted angle of 20°. The angle-tilting process was performed by object spectrum interpolation in reciprocal space [36].

Figure 4 shows the experimental results of the transmission configuration. In this experiment, we used a resolution target as the object. Figure 4(a) shows the recovered complex object exit wavefront $W(x, y)$ at the coded layer plane. The red dots in the left panels in Figs. 4(a1)–4(a3) represent the scanning positions of the coded image sensor; 3 \times 3 scanning steps were used in Fig. 4(a1), 8 \times 8 scanning steps in Fig. 4(a2), and 20 \times 20 scanning steps in Fig. 4(a3). Our implementation utilized a scanning step size of 800 μm . A random positional offset was added to avoid the raster grid pathology induced by periodic ambiguities [7]. With different numbers of scanning steps, the sizes of the synthesized images are 5.5 mm for Fig. 4(a1), 11 mm for Fig. 4(a2), and 20 mm for Fig. 4(a3). Figures 4(b1)–4(b3) show the refocused images at the object plane. For the 5.5-mm synthesized wavefront, we can resolve the 11- μm linewidth from the resolution target in Fig. 4(b1). For the 11-mm synthesized wavefront, we can resolve the 5.5- μm linewidth in Fig. 4(b2). For the 20-mm synthesized wavefront, we can resolve the 3- μm linewidth in Fig. 4(b2). Given the distance

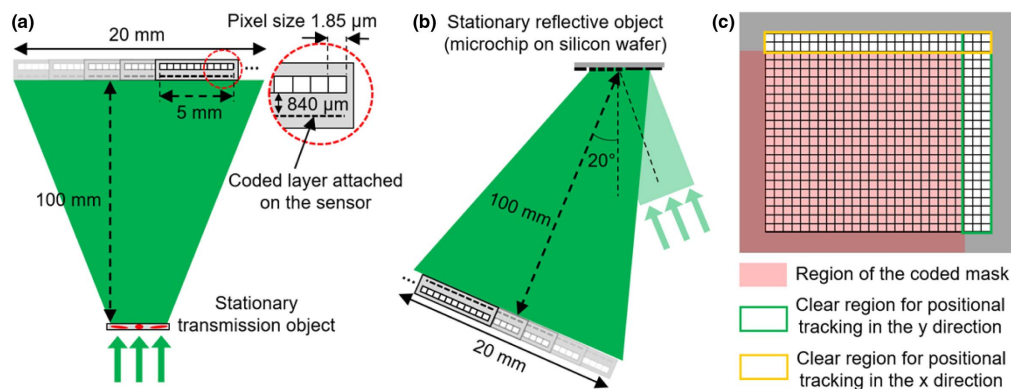


Fig. 3. Transmission and reflection configurations for SAP. For both configurations, the coded sensor is translated by a mechanical stage in the Fresnel zone. (a) Transmission configuration. The object exit wavefront synthesized at the intermediate aperture plane is backpropagated to the object plane for image recovery. (b) Reflection configuration. The coded sensor is translated in the direction perpendicular to the zero-order reflective beam. The recovered wavefront is then backpropagated to the object plane with a 20° tilted angle. (c) Employed coded image sensor. Two mask-free regions are used to track the positional shift in x and y directions.

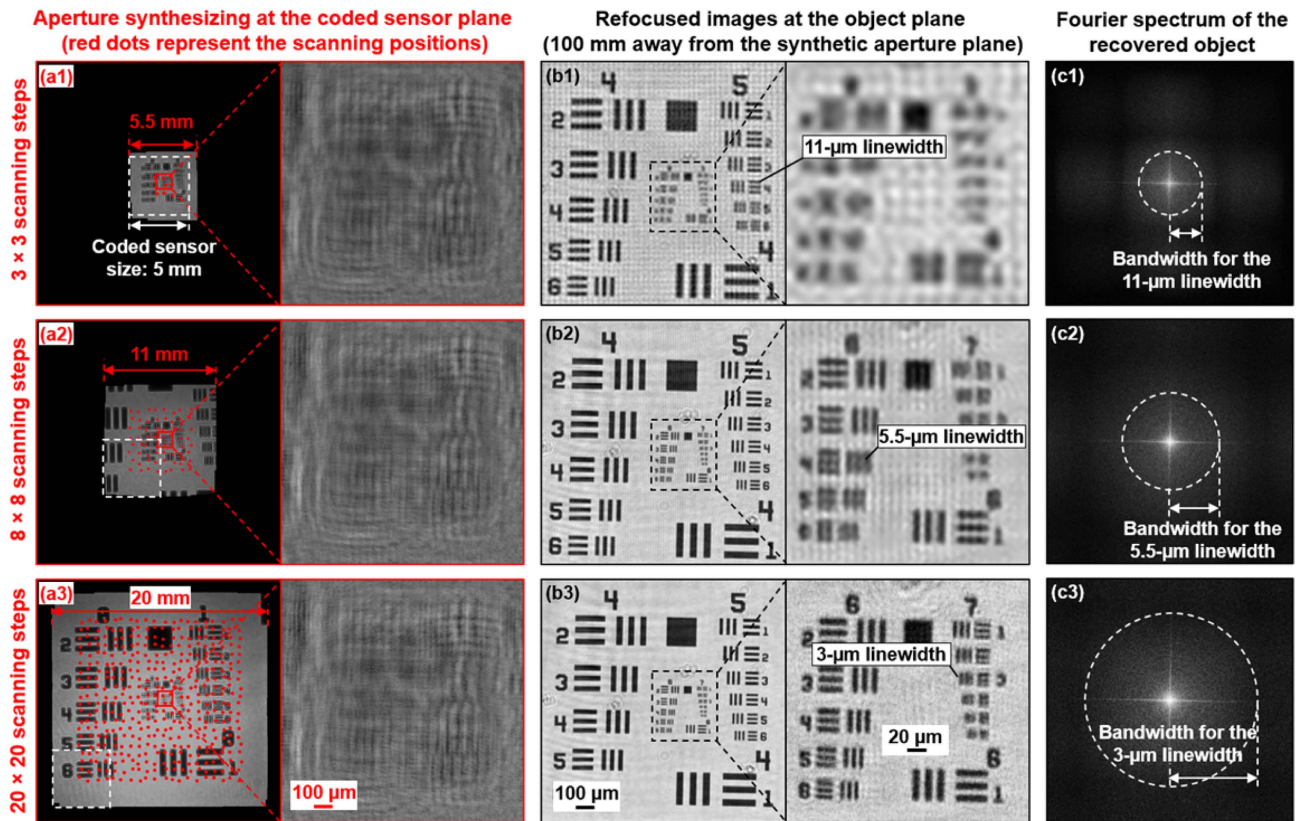


Fig. 4. Experimental validation of the transmission configuration of SAP. (a) Recovered wavefront $W(x, y)$ at the coded layer plane. By stitching together different numbers of measurements, we can synthesize images with a size of 5.5 mm (a1), 11 mm (a2), and 20 mm (a3). (b) Recovered wavefront backpropagated to the object plane. The recovered objects in (b1)–(b3) correspond to the synthesized wavefronts in (a1)–(a3). (c) Fourier spectra of the recovered objects. The expanded spatial-frequency bandwidths are highlighted by dashed circles.

between the object and the intermediate aperture plane, it can be contended that the achieved resolutions in Figs. 4(b1)–4(b3) are in good agreement with the corresponding detection NAs (determined by the spanning angles of the synthesized images at the intermediate aperture plane). In Fig. 4(c), we also plot the Fourier spectra of the recovered objects, where the dashed circles highlight the expanded spatial-frequency bandwidth in reciprocal space.

Figure 5 shows the experimental results of the reflection configuration. In this experiment, we used a microchip on a silicon wafer as the object. Figure 5(a) shows the recovered complex object exit wavefront at the coded layer plane. Similar to Fig. 4(a), the red dots in the left panels represent the scanning positions of the coded image sensor; 3×3 scanning steps were used in Fig. 5(a1), 8×8 scanning steps in Fig. 5(a2), and 20×20 scanning steps in Fig. 5(a3). The image sizes of the corresponding wavefronts are 5.5 mm, 11 mm, and 20 mm, respectively. We obtained the recovered images of the microchip in Fig. 5(b) by propagating the synthesized wavefronts to the object plane. In Fig. 5(c), we also show the corresponding phase images of the microchip. The improvement in resolution is clearly observed using the line trace in the right panels of Figs. 5(b1)–5(b3). Finally, we show the reconstruction results of another microchip in Fig. S3 in Ref. [35]. Figure S3(a) in Ref. [35] shows the recovered

large-field-of-view image at the object plane. Figure S3(b) in Ref. [35] shows the zoomed-in of the amplitude and phase. Figure S3(c) in Ref. [35] shows the height map of the recovered phase image.

Figures 4 and 5 validate the operation of the reported SAP approach. The sensor translation process in SAP synthesizes a large complex-valued wavefront at the intermediate aperture plane. For Figs. 4 and 5, we used eight iterations to recover the object exit wavefronts. By propagating this wavefront back to the object plane, we can widen the field of view in real space [Figs. 4(a) and 5(a)] and expand the spectral bandwidth in reciprocal space [Figs. 4(b) and 5(b)]. This unique feature enables us to obtain benefits from both conventional ptychography and FP. In Fig. S4 in Ref. [35], we compare the images at different planes in SAP. Figure S4(a) in Ref. [35] shows the raw images captured at the pixel-array plane. Figure S4(b) in Ref. [35] shows the synthesized images in the coded layer plane (intermediate aperture plane). Finally, Fig. S4(c) in Ref. [35] shows the images propagated back to the object plane.

A critical parameter for SAP reconstruction is the spatial overlap in between adjacent measurements. In Fig. S5, we analyze the SAP reconstructions with different spatial overlaps [35]. Figure S4(a) in Ref. [35] shows the SAP reconstructions using 400 raw measurements (20×20 scanning steps). Figures S4(b)–S4(d) in Ref. [35] show reconstructions

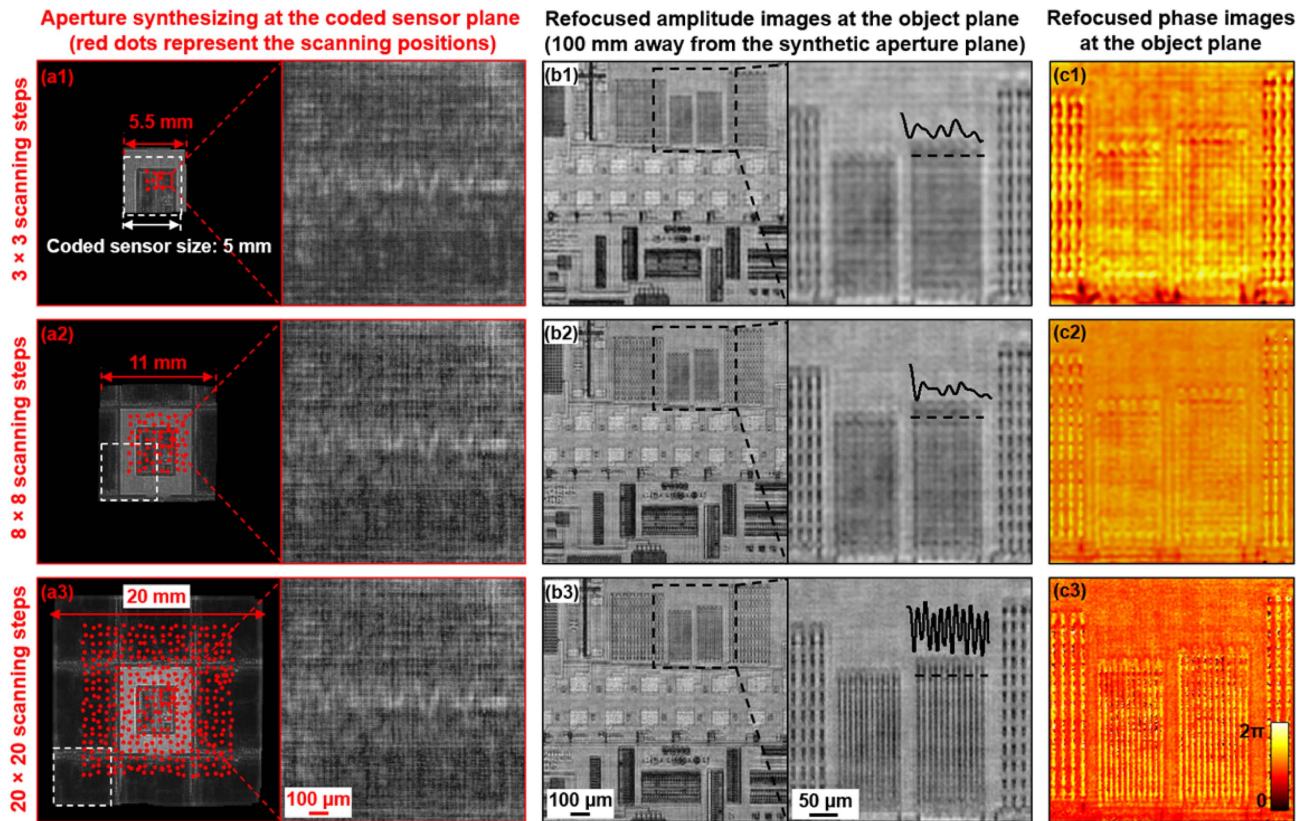


Fig. 5. Experimental validation of the reflection configuration of SAP. (a) Recovered wavefront $W(x,y)$ at the coded layer plane. By stitching together different numbers of measurements, we can synthesize images with a size of 5.5 mm (a1), 11 mm (a2), and 20 mm (a3). (b) Recovered wavefront backpropagated to the object plane with a tilted angle of $\sim 20^\circ$. (c) Recovered phase corresponding to (b).

with a reduced spatial overlap of $\sim 60\%$, $\sim 50\%$, and $\sim 25\%$, respectively. It can be observed that a large overlap helps to improve the reconstruction quality. The achieved resolution, on the other hand, remains largely unaffected by this overlap parameter.

Another advantage of the reported SAP approach is its capability of imaging axially extended 3D objects. In the reconstruction process, we aim to recover the object exit wavefront $W(x,y)$ instead of the object itself. Using the wavefront $W(x,y)$, we can backpropagate light waves to any plane along the axial direction for digital refocusing. In this backpropagation process, out-of-focus object information also contributes to the refocused plane. It is different from 3D tomography [37] or Fourier ptychographic diffraction tomography [25,26]. Figure S6 in Ref. [35] shows the experimental validation using an axially extended object. In this experiment, we used the same transmission setup as in Fig. 3(a). Two extra microscope slides were placed between the resolution target and coded image sensor. Figure S6(a) in Ref. [35] shows the recovered object exit wavefront at the intermediate aperture plane. In Figs. S6(b)–S6(d), we propagate the recovered wavefront to three different axial planes at $z = 40$ mm, 60 mm, and 100 mm, respectively [35]. It can be seen that the first microscope slide is in focus in Fig. S6(b1), the second slide is in focus in Fig. S6(c2), and the resolution target is in focus in Fig. S6(d3) [35]. Thus,

the reported SAP avoids the requirement of object thickness. The conventional thin sample requirement has been converted into the thin coded layer requirement in SAP.

4. CONCLUSION

We report a new CDI modality termed SAP. In SAP, we illuminate the entire stationary object using an extended plane wave and translate a coded image sensor at the far field for data acquisition. When operated in the Fresnel zone, the translation of the coded sensor can effectively widen the imaging field of view and expand the NA for object recovery, thereby achieving a combination of benefits from both conventional ptychography and FP. The lensless nature of SAP further allows it to be implemented with a variety of CDI setups with radiation sources from visible light, EUV, and X-rays, to electrons. We also show that SAP waives the thin sample requirement in conventional ptychography. The exit wavefront recovered at the intermediate aperture plane can be backpropagated to different axial planes for post-acquisition refocusing.

We identify the following development areas for SAP. First, the development of better algorithms to recover or refine different system parameters is highly desired. In the current mPIE routine, the step size depends on a hyperparameter α in line 11 of Fig. 2. It is possible to choose an optimal step size using the linear least-squares method [38]. A reconstruction routine that

corrects the tilt angle of the coded sensor can be a solution for building a robust SAP setup. Second, we envision implementing the SAP scheme in EUV and X-ray regimes. Identifying the defect in EUV masks is a challenging task, and the associated tools are expensive in semiconductor fabrication facilities. The reflection configuration discussed in Fig. 3(b) is a potential candidate for wafer inspection using EUV light. Third, our current demonstration is limited to one image sensor. It is straightforward to employ an array of coded sensors [18] to develop a high-throughput system.

The reported SAP offers a simple yet effective solution for sub-diffraction imaging via reference-free aperture synthesizing. The lensless nature of this modality further allows it to be implemented in a variety of CDIs that are generally limited by poor and aberrative lens elements. We envision that SAP will continue to grow and expand in various imaging applications.

Funding. National Science Foundation (2012140).

Acknowledgment. P. S. acknowledges the support of the Thermo Fisher Scientific fellowship.

Disclosures. The authors declare no competing financial interests.

Data Availability. The data and the reconstruction method are available from the corresponding author upon reasonable request. See Ref. [35] for the supporting content.

[†]These authors contributed equally to this paper.

REFERENCES

- J. Rodenburg and A. Maiden, "Ptychography," in *Springer Handbook of Microscopy* (Springer, 2019), pp. 819–904.
- M. Guizar-Sicairos and P. Thibault, "Ptychography: a solution to the phase problem," *Phys. Today* **74**, 42–48 (2021).
- W. Hoppe and G. Strube, "Diffraction in inhomogeneous primary wave fields. 2. Optical experiments for phase determination of lattice interferences," *Acta Crystallogr. A* **25**, 502–507 (1969).
- H. M. L. Faulkner and J. Rodenburg, "Movable aperture lensless transmission microscopy: a novel phase retrieval algorithm," *Phys. Rev. Lett.* **93**, 023903 (2004).
- M. Guizar-Sicairos and J. R. Fienup, "Phase retrieval with transverse translation diversity: a nonlinear optimization approach," *Opt. Express* **16**, 7264–7278 (2008).
- A. M. Maiden and J. M. Rodenburg, "An improved ptychographical phase retrieval algorithm for diffractive imaging," *Ultramicroscopy* **109**, 1256–1262 (2009).
- P. Thibault, M. Dierolf, O. Bunk, A. Menzel, and F. Pfeiffer, "Probe retrieval in ptychographic coherent diffractive imaging," *Ultramicroscopy* **109**, 338–343 (2009).
- X. Ou, G. Zheng, and C. Yang, "Embedded pupil function recovery for Fourier ptychographic microscopy," *Opt. Express* **22**, 4960–4972 (2014).
- P. Thibault and A. Menzel, "Reconstructing state mixtures from diffraction measurements," *Nature* **494**, 68–71 (2013).
- D. J. Batey, D. Claus, and J. M. Rodenburg, "Information multiplexing in ptychography," *Ultramicroscopy* **138**, 13–21 (2014).
- P. Song, R. Wang, J. Zhu, T. Wang, Z. Bian, Z. Zhang, K. Hoshino, M. Murphy, S. Jiang, and C. Guo, "Super-resolved multispectral lensless microscopy via angle-tilted, wavelength-multiplexed ptychographic modulation," *Opt. Lett.* **45**, 3486–3489 (2020).
- Y. Yao, Y. Jiang, J. Klug, Y. Nashed, C. Roehrig, C. Preissner, F. Marin, M. Wojcik, O. Cossairt, and Z. Cai, "Broadband X-ray ptychography using multi-wavelength algorithm," *J. Synchrotron. Radiat.* **28**, 309–317 (2021).
- A. M. Maiden, M. J. Humphry, and J. Rodenburg, "Ptychographic transmission microscopy in three dimensions using a multi-slice approach," *J. Opt. Soc. Am. A* **29**, 1606–1614 (2012).
- A. M. Maiden, M. J. Humphry, F. Zhang, and J. M. Rodenburg, "Superresolution imaging via ptychography," *J. Opt. Soc. Am. A* **28**, 604–612 (2011).
- M. Odstroil, P. Baksh, S. Boden, R. Card, J. Chad, J. Frey, and W. Brocklesby, "Ptychographic coherent diffractive imaging with orthogonal probe relaxation," *Opt. Express* **24**, 8360–8369 (2016).
- P. Song, C. Guo, S. Jiang, T. Wang, P. Hu, D. Hu, Z. Zhang, B. Feng, and G. Zheng, "Optofluidic ptychography on a chip," *Lab Chip* **21**, 4549–4556 (2021).
- S. Jiang, C. Guo, T. Wang, J. Liu, P. Song, T. Zhang, R. Wang, B. Feng, and G. Zheng, "Blood-coated sensor for high-throughput ptychographic cytometry on a Blu-Ray disc," *ACS Sens.* **7**, 1058–1067 (2022).
- S. Jiang, C. Guo, P. Song, N. Zhou, Z. Bian, J. Zhu, R. Wang, P. Dong, Z. Zhang, J. Liao, J. Yao, B. Feng, M. Murphy, and G. Zheng, "Resolution-enhanced parallel coded ptychography for high-throughput optical imaging," *ACS Photon.* **8**, 3261–3271 (2021).
- S. Jiang, C. Guo, P. Song, T. Wang, R. Wang, T. Zhang, Q. Wu, R. Pandey, and G. Zheng, "High-throughput digital pathology via a handheld, multiplexed, and AI-powered ptychographic whole slide scanner," *Lab Chip* (2022).
- S. Jiang, C. Guo, Z. Bian, R. Wang, J. Zhu, P. Song, P. Hu, D. Hu, Z. Zhang, K. Hoshino, B. Feng, and G. Zheng, "Ptychographic sensor for large-scale lensless microbial monitoring with high spatiotemporal resolution," *Biosens. Bioelectron.* **196**, 113699 (2022).
- S. Jiang, J. Zhu, P. Song, C. Guo, Z. Bian, R. Wang, Y. Huang, S. Wang, H. Zhang, and G. Zheng, "Wide-field, high-resolution lensless on-chip microscopy via near-field blind ptychographic modulation," *Lab Chip* **20**, 1058–1065 (2020).
- L. Loetgering, S. Witte, and J. Rothhardt, "Advances in laboratory-scale ptychography using high harmonic sources," *Opt. Express* **30**, 4133–4164 (2022).
- F. Pfeiffer, "X-ray ptychography," *Nat. Photonics* **12**, 9–17 (2018).
- G. Zheng, R. Horstmeyer, and C. Yang, "Wide-field, high-resolution Fourier ptychographic microscopy," *Nat. Photonics* **7**, 739–745 (2013).
- R. Horstmeyer, J. Chung, X. Ou, G. Zheng, and C. Yang, "Diffraction tomography with Fourier ptychography," *Optica* **3**, 827–835 (2016).
- C. Zuo, J. Sun, J. Li, A. Asundi, and Q. Chen, "Wide-field high-resolution 3D microscopy with Fourier ptychographic diffraction tomography," *Opt. Lasers Eng.* **128**, 106003 (2020).
- S. Dong, R. Horstmeyer, R. Shiradkar, K. Guo, X. Ou, Z. Bian, H. Xin, and G. Zheng, "Aperture-scanning Fourier ptychography for 3D refocusing and super-resolution macroscopic imaging," *Opt. Express* **22**, 13586–13599 (2014).
- J. Holloway, Y. Wu, M. K. Sharma, O. Cossairt, and A. Veeraraghavan, "SAVI: synthetic apertures for long-range, subdiffraction-limited visible imaging using Fourier ptychography," *Sci. Adv.* **3**, e1602564 (2017).
- K. Wakonig, A. Diaz, A. Bonnin, M. Stampanoni, A. Bergamaschi, J. Ihli, M. Guizar-Sicairos, and A. Menzel, "X-ray Fourier ptychography," *Sci. Adv.* **5**, eaav0282 (2019).
- P. Thibault, M. Dierolf, A. Menzel, O. Bunk, C. David, and F. Pfeiffer, "High-resolution scanning x-ray diffraction microscopy," *Science* **321**, 379–382 (2008).
- E. H. Tsai, I. Usov, A. Diaz, A. Menzel, and M. Guizar-Sicairos, "X-ray ptychography with extended depth of field," *Opt. Express* **24**, 29089–29108 (2016).
- P. Song, S. Jiang, H. Zhang, Z. Bian, C. Guo, K. Hoshino, and G. Zheng, "Super-resolution microscopy via ptychographic structured modulation of a diffuser," *Opt. Lett.* **44**, 3645–3648 (2019).

33. A. E. Tippie, A. Kumar, and J. R. Fienup, "High-resolution synthetic-aperture digital holography with digital phase and pupil correction," *Opt. Express* **19**, 12027–12038 (2011).
34. A. Maiden, D. Johnson, and P. Li, "Further improvements to the ptychographical iterative engine," *Optica* **4**, 736–745 (2017).
35. P. Song, S. Jiang, T. Wang, C. Guo, R. Wang, T. Zhang, and G. Zheng, <https://figshare.com/s/00579856fca61ba781e1> (2022).
36. S. Jiang, C. Guo, P. Hu, D. Hu, P. Song, T. Wang, Z. Bian, Z. Zhang, and G. Zheng, "High-throughput lensless whole slide imaging via continuous height-varying modulation of a tilted sensor," *Opt. Lett.* **46**, 5212–5215 (2021).
37. G. Zheng, C. Kolner, and C. Yang, "Microscopy refocusing and dark-field imaging by using a simple LED array," *Opt. Lett.* **36**, 3987–3989 (2011).
38. M. Odstrčil, A. Menzel, and M. Guizar-Sicairos, "Iterative least-squares solver for generalized maximum-likelihood ptychography," *Opt. Express* **26**, 3108–3123 (2018).